A&A, 690, A70 (2024)
https://doi.org/10.1051/0004-6361/202450375
© The Authors 2024

Astronomy & Astrophysics

Uncovering the physical origin of the prominent Lyman-α emission and absorption in GS9422 at $z = 5.943$

Chamilla Terp[1,2,⋆], Kasper E. Heintz[1,2,3], Darach Watson[1,2], Gabriel Brammer[1,2], Adam Carnall[4], Joris Witstok[5,6], Renske Smit[7], and Simone Vejlgaard[1,2]

[1] Cosmic Dawn Center (DAWN), Rådmandsgade 64, 2200 Copenhagen N, Denmark
[2] Niels Bohr Institute, University of Copenhagen, Jagtvej 128, 2200 Copenhagen N, Denmark
[3] Department of Astronomy, University of Geneva, Chemin Pegasi 51, 1290 Versoix, Switzerland
[4] Institute for Astronomy, University of Edinburgh, Royal Observatory, Edinburgh EH9 3HJ, UK
[5] Kavli Institute for Cosmology, University of Cambridge, Madingley Road, Cambridge CB3 0HA, UK
[6] Cavendish Laboratory, University of Cambridge, 19 JJ Thomson Avenue, Cambridge CB3 0HE, UK
[7] Astrophysics Research Institute, Liverpool John Moores University, Liverpool L35 UG, UK

Received 15 April 2024 / Accepted 2 August 2024

ABSTRACT

We present a comprehensive spectrophotometric analysis of galaxy GS9422 from the JADES GTO survey located at $z = 5.943$, anomalously showing a simultaneous strong Lyα emission feature and damped Lyα absorption (DLA), based on JWST NIRSpec and NIRCam observations. The best-fit modeling of the spectral energy distribution (SED) reveals a young, low-mass ($\log(M_\star/M_\odot) = 7.80\pm0.01$) galaxy, with a mass-weighted mean age of the stellar population of $(10.90^{+0.07}_{-0.12})$ Myr. The identified strong nebular emission lines suggest a highly ionized ($O_{32} = 59$), low-metallicity ($12 + \log(O/H) = 7.78 \pm 0.10$) star-forming galaxy with a star-formation rate (SFR) of $(8.2 \pm 2.8)\,M_\odot\,\mathrm{yr}^{-1}$ over a compact surface area $A_e = 1.85\,\mathrm{kpc}^2$, typical for galaxies at this epoch. This corresponds to an intense SFR surface density of $\log(\Sigma_{SFR}/M_\odot\,\mathrm{yr}^{-1}\,\mathrm{kpc}^{-2}) = 1.14 \pm 0.30$. We carefully modeled the rest-frame UV NIRSpec Prism spectrum around the Lyα edge, finding that the Lyα emission-line redshift is consistent with the longer-wavelength recombination lines and an escape fraction of $f_{esc,Ly\alpha} = 30\%$ but that the broad DLA feature is not able to converge on the same redshift. Instead, our modeling suggests $z_{abs} = 5.40 \pm 0.10$, the exact redshift of a newly identified protocluster in nearby projection to the target galaxy. We argue that most of the H I gas producing the strong Lyα damping wing must be unassociated with the galaxy itself, and thus may indicate that we are probing the cold, dense circumcluster medium of this massive galaxy overdensity. These results provide an alternative solution to the recent claims of continuum nebular emission or an obscured active galactic nucleus dominating the rest-frame UV parts of the spectrum, and provide further indications that strong DLAs might preferentially be associated with galaxy overdensities.

Key words. galaxies: clusters: general – galaxies: clusters: intracluster medium – galaxies: evolution – galaxies: formation – galaxies: high-redshift

1. Introduction

The first billion years of cosmic time saw the transition from primordial, neutral hydrogen and helium atoms into the first stars and galaxies, the synthesis of heavier elements in stellar cores, and the eventual reionization of the Universe. With the launch of the *James Webb* Space Telescope (JWST) and its powerful near-infrared capabilities, we are now able to study and constrain these processes within this critical era of the early Universe (Robertson 2022). Spectroscopic observations with JWST/NIRSpec (Jakobsen et al. 2022) have in particular been paramount in spectroscopically identifying the most distant galaxies to date, at $z \approx 11$–13 (Curtis-Lake et al. 2023; Wang et al. 2023; Fujimoto et al. 2023; Bunker et al. 2023), and charting the chemical enrichment of galaxies at $z > 6$ (e.g., Schaerer et al. 2022; Arellano-Córdova et al. 2022; Taylor et al. 2022; Brinchmann 2023; Curti et al. 2023; Katz et al. 2023; Rhoads et al. 2023; Trump et al. 2023; Heintz et al. 2023a; Nakajima et al. 2023; Langeroodi et al. 2023; Sanders et al. 2024). These early observations revealed that galaxies at $z > 7$ appear chemically "diluted" based on the negative offset of their gas-phase metallicities from the otherwise fundamental-metallicity relation (Heintz et al. 2023b), although the exact redshift for this transition is still debated (Nakajima et al. 2023; Curti et al. 2024). This indicates that JWST is starting to uncover the formation phase of galaxies at a point when they are still intimately connected to the intergalactic medium (IGM) and experiencing excessive H I gas overflow.

A significant fraction of galaxies at $z > 8$ have been discovered with extremely strong damped Lyman-α (Lyα) absorption (DLA; Heintz et al. 2024a, see also Umeda et al. 2023; D'Eugenio et al. 2024), in excess of the damping wings expected for a largely neutral IGM at these redshifts (Miralda-Escudé 1998; McQuinn et al. 2008; Keating et al. 2023). These observations imply high H I gas column densities, $N_{HI} \gtrsim 10^{22}\,\mathrm{cm}^{-2}$, and covering fractions, and may be prevalent in $\gtrsim$65% of the galaxy population at $z > 8$ (Heintz et al. 2024b). At lower redshifts, near the end of reionization at $z \approx 6$, the fraction of galaxies showing strong integrated DLAs decreases to $\approx$30% and represents only the youngest star-forming systems that are yet to substantially ionize their surrounding gas or process

⋆ Corresponding author; bmx626@alumni.ku.dk

Open Access article, published by EDP Sciences, under the terms of the Creative Commons Attribution License (https://creativecommons.org/licenses/by/4.0), which permits unrestricted use, distribution, and reproduction in any medium, provided the original work is properly cited.
This article is published in open access under the Subscribe to Open model. Subscribe to A&A to support open access publication.

most of the neutral, atomic hydrogen gas into molecules and stars. Later, at the peak of cosmic star formation at $z \sim 2$–3, DLAs are only observed in rare cases of star-forming galaxies (Shapley et al. 2003; James et al. 2014; Erb et al. 2019; Lin et al. 2023) and with H I abundances orders of magnitude lower than those observed at $z > 6$.

As part of the JWST/NIRSpec PRImordial gas Mass AssembLy (PRIMAL) survey (JWST-PRIMAL; Heintz et al. 2024b) targeting galaxies during the reionization epoch at $z > 5.5$ with robust spectroscopic redshifts and continuum sensitivity near Lyα, we identified one intriguing source showing strong (Lyα) emission and DLA at $z = 5.94$. Intuitively, this seems to counter the general observed trends and strains the physical interpretation of substantial H I gas producing strong Lyα damping wings while at the same time enabling the escape of Lyα photons. Here, we thus aim to characterize the source in detail and suggest some physical scenarios that might explain these extreme observables. We note that this particular case has also been studied by Cameron et al. (2023), who present evidence of the rest-frame UV shape of this galaxy spectrum being dominated by nebular two-photon emission. However, the high stellar temperatures required (100 000 K), the observed weak rest-optical emission lines and ionizing photon production efficiency, and relatively high gas-phase metallicity make this finding ambiguous (Chen et al. 2023). Other studies suggest that this source hosts an obscured active galactic nucleus (AGN) where the rest-UV light reflects a central young stellar disk (Tacchella et al. 2024; Li et al. 2024), further motivating a more detailed analysis of this particular source.

We have structured the paper as follows. In Sect. 2 we describe the photometric and spectroscopic observations, and in Sect. 3 we present our analysis and results. In Sect. 4 we place the characteristics of the source into context, classify the likely underlying source of emission, and present an alternative scenario that can resolve this rare conundrum of a simultaneous strong (Lyα) emission and DLA feature observed in the integrated galaxy spectrum. Throughout the paper we assume concordance flat Λ cold dark matter (CDM) cosmology, with $H_0 = 67.4\,\mathrm{km\,s^{-1}\,Mpc^{-1}}$, $\Omega_\mathrm{m} = 0.315$, and $\Omega_\Lambda = 0.685$ (Planck Collaboration VI 2020).

2. JWST observations

The source (hereafter "GS9422") was observed with JWST/NIRSpec (Jakobsen et al. 2022) as part of the GTO JWST Advanced Deep Extragalactic Survey (JADES, prog. ID: 1210, PI: Luetzendorf) with MSA source ID 13176, as detailed in Eisenstein et al. (2023) and Bunker et al. (2024). The observations were separated into 28 hours of integration in each of the medium-resolution gratings G140M/F070LP, G235M/F170LP, and G395M/F290LP. The Prism spectrum covers the entire wavelength range of NIRSpec from 0.7–5.3 μm at a resolving power $\mathcal{R} \approx 100$. The NIRSpec grating covers smaller bandwidths but at a spectral resolution of $\mathcal{R} \approx 1000$. We adopted the reduced and processed spectra delivered by the DAWN JWST Archive (DJA)[1], reduced through the custom-made MSAExp pipeline (Brammer 2023)[2]. Further details of the reduction process are provided in Heintz et al. (2024b). Throughout this study, we mainly considered the NIRSpec Prism observations for the continuum modeling of the spectral energy distribution (SED) and the medium-resolution grating spectra for the emission line fluxes and kinematics.

We further included JWST/NIRCam (Rieke et al. 2023) imaging of the source obtained as part of JADES (Eisenstein et al. 2023) in the seven broadband filters: F090W, F115W, F150W, F200W, F277W, F356W, and F444W. We adopted the photometry listed in DJA for all filters, derived in a 0.″5 circular aperture around the centroid of the source at RA (J2000) = $03^\mathrm{h}32^\mathrm{m}29.2^\mathrm{s}$ and Dec (J2000) = $-27°47'51.48''$. The images were processed using Grizli (Brammer et al. 2022)[3], which astrometrically calibrates each field to the *Gaia*-DR3 reference frame and drizzles the images to a common pixel scale of 0.″04/pixel (see Valentino et al. 2023, for further details). We further used photometry to rescale the 1D spectra to account for potential slit losses and improve the absolute flux calibration of the spectra.

3. Analysis and results

3.1. Redshift and line fluxes

Based on the extracted 1D JWST/NIRSpec medium-resolution grating spectra, we detected and derived the line fluxes of the following nebular and auroral emission lines: Lyα, [C IV] $\lambda\lambda$1548, 1550, [He II] λ1640, [O III] λ1666, [O II] $\lambda\lambda$3727, 3729, H9, [Ne III]λ3869, [He I]λ3889, [O III]λ4363, 4959, and 5007, as well as the Balmer lines, Hα and Hβ (some of these lines are also detected in the Prism spectrum). We further detected and derived line fluxes for [O I]λ6300 and Hγ in the Prism spectrum. For each separate grating spectrum, we modeled the continuum with a simple polynomial and the emission features with Gaussian line profiles, tying the redshift, z_spec, and the line full width half maximum (FWHM) across transitions. This assumes that the emission lines all originate from and trace the same ionized gas in the star-forming region of the galaxy. We derived a spectroscopic redshift of $z_\mathrm{spec} = 5.943 \pm 0.001$ and a line FWHM = $218 \pm 144\,\mathrm{km\,s^{-1}}$. The best-fit line model is shown in Fig. 1, and the derived line fluxes are summarized in Table 1.

3.2. Star-formation rate and rest-frame UV characteristics

The derived ratios of the three strongest Balmer lines, Hβ/Hγ = 2 ± 0.08 and Hα/Hβ = 2.77 ± 0.08, are consistent with the theoretically predicted values assuming a Case B recombination scenario with $T_\mathrm{e} = 10^4$ K (Osterbrock & Ferland 2006), indicating negligible dust attenuation. We caution, however, that Hα is not covered by any of the grating spectra, so the ratio Hα/Hβ was measured using the Hα line flux derived from the Prism spectrum. We further integrated the spectral region covering Hβ and the [O III] $\lambda\lambda$4960, 5008 doublet, yielding a joint equivalent width (EW) of 2266.4 ± 71.1 Å. This is among the highest 16th percentile distribution of the full JWST-PRIMAL sample, revealing an intensely star-forming galaxy.

We derived the star-formation rate (SFR) following Kennicutt (1998) based on the Hα line luminosity,

$$\mathrm{SFR}_{\mathrm{H}\alpha}\,(M_\odot\,\mathrm{yr}^{-1}) = 5.5 \times 10^{-42}\,L_{\mathrm{H}\alpha}\,(\mathrm{erg\,s}^{-1}), \quad (1)$$

assuming the initial mass function (IMF) from Kroupa (2001). This is more top-heavy than the typical adopted Salpeter or Chabrier IMFs, and thus likely more appropriate for high-redshift galaxies (e.g., Steinhardt et al. 2023). This yields an

[1] https://dawn-cph.github.io/dja/index.html
[2] Version 0.6.17; https://doi.org/10.5281/zenodo.7299500
[3] https://doi.org/10.5281/zenodo.6672538

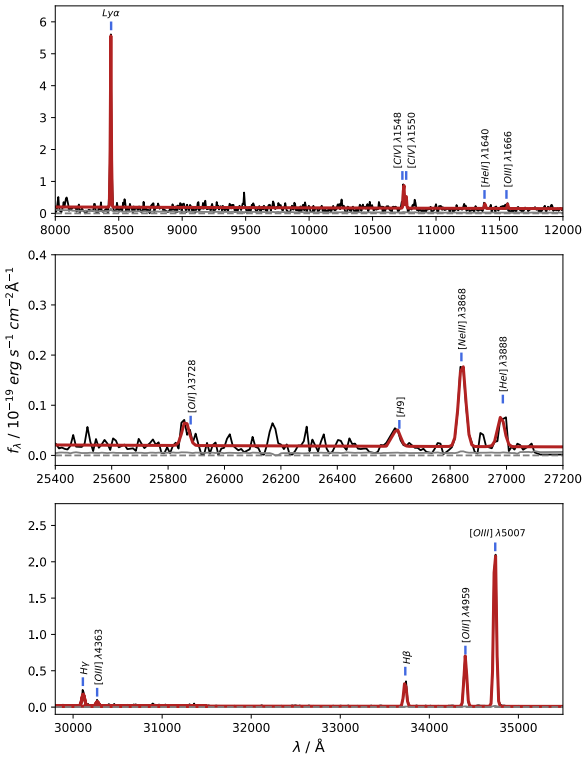

Fig. 1. Zoomed-in views of the regions of medium-resolution gratings with the main nebular and auroral emission line transitions marked. The best-fit continuum and Gaussian profiles to each line transition are shown by the solid red line.

SFR of $8.20 \pm 0.15\,M_\odot\,\mathrm{yr}^{-1}$, indicating a significant star formation activity. Assuming a different IMF introduces an additional ≈30% systematic uncertainty on the SFR, which we propagated to the SFR in the following analysis. We further note that the measured line width (≈218 km s^{-1}) and the derived [O III] λ5007/Hβ versus [O I] λ6300/Hβ line flux ratios do not indicate any robust signatures of an AGN based on the demarcation line from Kewley et al. (2001). This source may thus simply be a highly ionized star-forming galaxy, as also supported by the high ionization parameter, O_{32} = [O III]5008/[O II] λ3728 = 59 ± 20. We note, however, that this demarcation may not be applicable at high redshifts (Übler et al. 2023; Calabro et al. 2024), and indeed, for this particular source, studies suggests an AGN origin for this source based on the emission line flux and continuum (Scholtz et al. 2023; Tacchella et al. 2024).

We inferred the absolute UV magnitude of the source by integrating the flux density of the photometrically calibrated spectra in the region around rest frame ≈1500 Å, finding $M_{\rm UV} = -19.56 \pm 0.05$ mag or $L_{\rm UV} = (3.15 \pm 0.16) \times 10^{28}$ erg Hz s^{-1}. We derived the equivalent SFR from the UV luminosity again following Kennicutt (1998),

$$\mathrm{SFR_{UV}}\,(M_\odot\,\mathrm{yr}^{-1}) = 10^{-28}\,L_{\rm UV}\,(\mathrm{erg\,Hz\,s^{-1}}), \quad (2)$$

here assuming 1/10 solar metallicity. This yields $\mathrm{SFR_{UV}} = 3.2 \pm 1.2\,M_\odot\,\mathrm{yr}^{-1}$, consistent within 2σ of the estimate from the Hα recombination line. From the spectra, we further derived the ionizing photon production efficiency of the source, $\xi_{\rm ion}$ (Bouwens et al. 2016). Following Matthee et al. (2023), we derived

$$\xi_{\rm ion}\,(\mathrm{Hz\,erg^{-1}}) = \frac{L_{\rm H\beta}\,(\mathrm{erg\,s^{-1}})}{c_{\rm H\beta}(\mathrm{erg})\;L_{\rm UV}(\mathrm{erg\,s^{-1}\,Hz^{-1}})}, \quad (3)$$

Table 1. Line flux measurements.

	PRISM	G140M	G235M	G395M
Lyα	92.8 ± 1.0	52.5 ± 1.2	–	–
[CIV] λ1548	–	8.2 ± 1.0	–	–
[CIV] λ1550	33.6 ± 2.1	4.3 ± 1.0	–	–
[HeII] λ1640	–	1.6 ± 1.0	–	–
[OIII] λ1666	–	1.4 ± 1.0	–	–
[OII] $\lambda\lambda$3728	–	–	1.5 ± 0.3	–
H9	–	–	1.0 ± 0.3	–
[NeIII] λ3869	18.2 ± 0.8	–	5.2 ± 0.3	–
[HeI] λ3889	–	–	2.0 ± 0.3	–
Hγ	–	–	–	6.6 ± 0.2
[OIII] λ4363	–	–	–	2.4 ± 0.2
Hβ	17.5 ± 0.9	–	–	13.2 ± 0.3
[OIII] λ4959	32.8 ± 0.1	–	–	27.1 ± 0.3
[OIII] λ5007	88.7 ± 0.4	–	–	88.7 ± 0.3
[OI] λ6300	0.5 ± 0.2	–	–	–
Hα	36.6 ± 0.7	–	–	–

Notes. Line flux measurements reported in units of $\times 10^{-19}$ erg s^{-1} cm^{-2}.

where $c_{\rm H\beta} = 4.86 \times 10^{-13}$ erg is the Hβ line-emission coefficient, assuming a Case B recombination scenario with $T_{\rm e} = 10^4$ K and a zero escape fraction of ionizing Lyman continuum (LyC) photons, $f_{\rm esc}^{\rm LyC} = 0$ (e.g., Schaerer 2003). This yields $\log \xi_{\rm ion} = 25.62 \pm 0.02$, which is among the highest known efficiency rates of galaxies at $z \gtrsim 6$ (e.g., Matthee et al. 2023; Atek et al. 2023; Fujimoto et al. 2023; Heintz et al. 2024b) and slightly above the canonical value on average required to ionize the IGM (Robertson et al. 2013).

Finally, we measured the spatial size of GS9422 in the F105W filter (rest-frame UV ≈1500 Å) with a 2D Gaussian model, which provides a good match to the apparent simple morphology of the source (see Fig. 2). From the best-fit 2D Gaussian model, we extracted semimajor and semiminor axes, a' and b', and derived an effective half-light UV radius $R_{\rm eff,UV} = \sqrt{a'b'} = 0\farcs8$, which corresponds to a projected physical size of 0.59 kpc at $z = 5.943$. The intense SFR and small physical size indicate that this source has an SFR surface density, $\log(\Sigma_{\rm SFR}/M_\odot\,\mathrm{yr}^{-1}\,\mathrm{kpc}^{-2}) = 1.14 \pm 0.30$, among the highest known of the local galaxy population (e.g., Kennicutt & Evans 2012).

3.3. Gas-phase metallicity

In the $\mathcal{R} \approx 1000$ grating spectrum, we were able to detect and resolve the auroral line [O III] λ4363 from Hγ. This enabled us to determine a temperature-sensitive estimate of the gas-phase metallicity of this galaxy (the so-called direct $T_{\rm e}$ method) in combination with the nebular lines [O III] $\lambda\lambda$4960, 5008 and Hβ emission lines. Following the iterations outlined in Izotov et al. (2006), we inferred an electron temperature $T_{\rm e} = (1.60 \pm 0.15) \times 10^4$ K and oxygen abundance of $12 + \log(\mathrm{O/H}) = 7.78 \pm 0.10$, for any electron densities $n_{\rm e} < 10^4\,\mathrm{cm}^{-3}$ (common for most H II regions, see Fig. 3). This corresponds to a metallicity that is about 10% of the solar metallicity (for $12 + \log(\mathrm{O/H})_\odot = 8.7$; Asplund et al. 2009), common for galaxies at the same redshift (Langeroodi et al. 2023; Heintz et al. 2023b; Curti et al. 2024) for the given SFR and stellar mass (see Sect. 3.4 below). Our estimate is, moreover, consistent with that derived by Cameron et al. (2023).

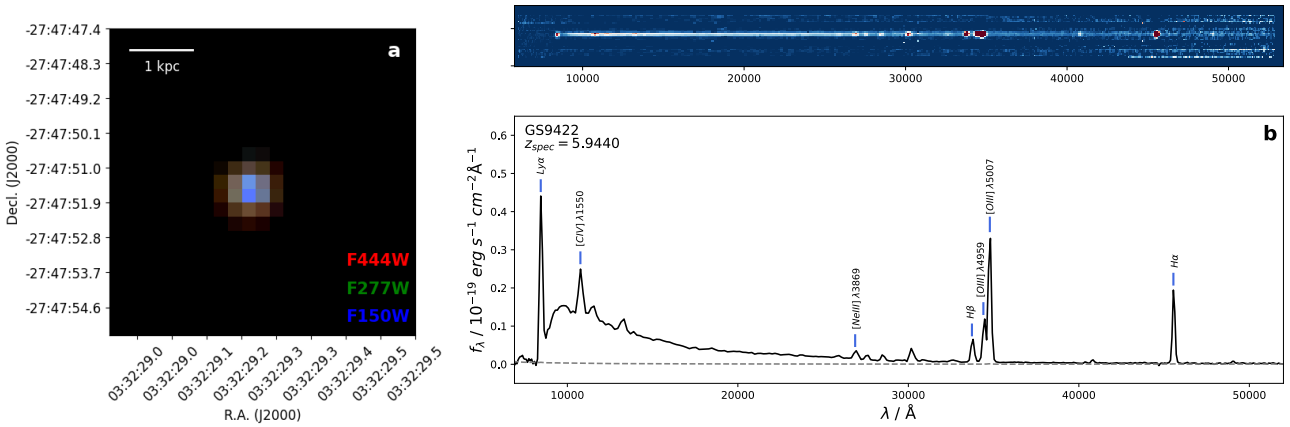

Fig. 2. False-RGB plot (a) and NIRSpec spectrum of GS9422 (b). (a) False-RGB-plot zoomed in on GS9422 based on the JWST/NIRCam filters: F444W (red), F277W (green), and F150W (blue). Physical scale is calculated in the source plane. (b) JWST/NIRSpec Prism spectrum with the most prominent nebular and auroral emission lines marked. Top panel shows the 2D trace spectrum.

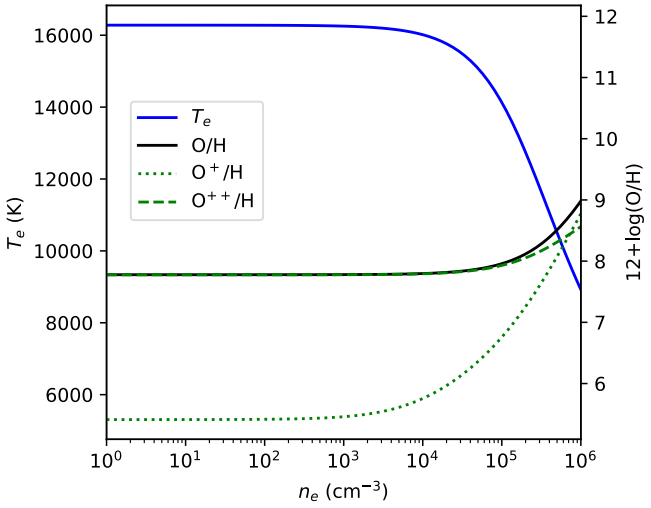

Fig. 3. Electron temperature, T_e, as a function of density, n_e, based on the observed nebular and auroral [O III], [O II], and Hβ line fluxes following the prescription by Izotov et al. (2006). The derived electron temperature is $T_e = (1.6\pm0.15)\times10^4$ K, indicating an oxygen abundance of $12+\log(O/H) = 7.78\pm0.10$ for any electron densities $n_e < 10^4$ cm^{-3}.

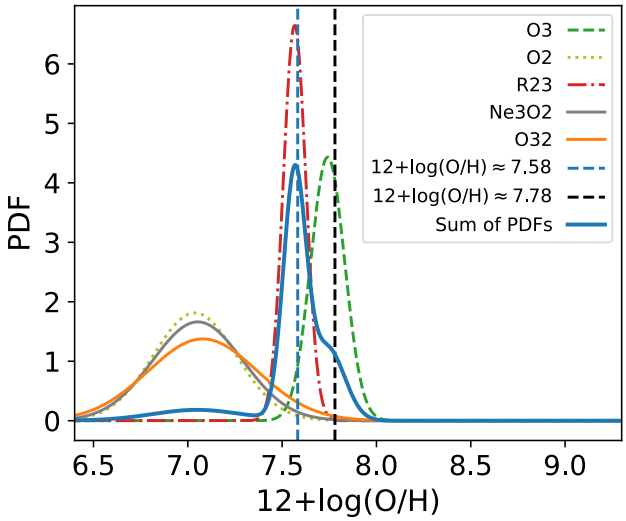

Fig. 4. Normalized probability density functions (PDFs) for each metallicity calculation. Blue and black vertical lines represent the 12 + log(O/H) values calculated using the strong-line calibrations method by Sanders et al. (2024) and T_e method, respectively.

We used the metallicity derived from the direct T_e method to evaluate the various strong-line ratios inferred for galaxies at $z > 6$ (e.g., Nakajima et al. 2023; Sanders et al. 2024). Specifically, we tested the more conservative approach by Heintz et al. (2024b), deriving the joint posterior distribution function (PDF) from each applicable strong-line diagnostic inversely weighted by the scatter for each relation, and represented the final metallicity as the median and 16th to 84th percentiles of the joint PDF. We assumed the single set of calibrations from Sanders et al. (2024) and show the individual and joint PDFs in Fig. 4. The width of these PDFs includes both the statistical uncertainties from the measured line flux ratios and the systematic uncertainties from the particular line calibration used. Based on this approach, we find a median 12 + log(O/H) = 7.58 of the distribution, with 16th to 84th percentiles of 7.54 to 7.63. This is consistent within 1σ with the measurement from the direct T_e method. We note that the O_3 calibration shows the best qualitative agreement with the direct T_e method for this particular case, likely due to the high ionization parameter of the source. Assuming instead the R23 calibration, for instance, would underestimate the actual metallicity at more than 3σ. This more conservative approach thus seems to optimally take into account the uncertainties related to each individual calibrator.

3.4. Spectrophotometric SED modeling

We performed joint spectrophotometric modeling of the JWST/NIRSpec and NIRCam data to derive the SED of the source and extracted additional physical parameters using BAGPIPES (Carnall et al. 2018). We modified the default BAGPIPES framework to incorporate an additional Lyα absorption component that allowed us to additionally constrain the H I column density in the SED model of the galaxy. This is particularly important for this galaxy as the DLA feature dominates the continuum flux at rest-frame UV wavelengths near the Lyα emission line profile. The Lyα optical depth from local interstellar medium (ISM) H I gas is described through the Voigt-Hjerting absorption profile following the analytical approxima-

tion derived by Tepper-García (2006) as shown in Eq. (4):

$$\tau_{\rm ISM}(\lambda) = C\, a\, H(a,x)\, N_{\rm H\,I}. \quad (4)$$

Here, C is the photon absorption constant, a is the damping parameter, and $H(a,x)$ is the Voigt-Hjerting function. We further modeled the optical depth due to the Gunn-Peterson effect from an increasingly neutral IGM, given by Miralda-Escude et al. (2000) with

$$\tau_{\rm GP}(z) = 1.8\times10^5\, h^{-1}(\Omega_{\rm DM,0})^{-1/2} x_{\rm HI}\left(\frac{\Omega_{\rm m,0}\,h^2}{0.02}\right)\left(\frac{1+z}{7}\right)^{3/2}. \quad (5)$$

We modified this following the formalism of Totani et al. (2006)

$$\tau_{\rm IGM}(\lambda,z) = \frac{x_{\rm H\,I} R_\alpha \tau_{\rm GP}(z_{\rm spec})}{\pi}\left(\frac{1+z_{\rm abs}}{1+z_{\rm spec}}\right)^{3/2} \times\left[I\left(\frac{1+z_{\rm IGM,u}}{1+z_{\rm abs}}\right) - I\left(\frac{1+z_{\rm IGM,l}}{1+z_{\rm abs}}\right)\right], \quad (6)$$

where $z_{\rm abs}$ is the observed redshift of the neutral gas, $x_{\rm H\,I}$ is the average neutral to total hydrogen fraction of the IGM (assumed to be 0.01), and $R_\alpha = \Lambda_\alpha \lambda_{{\rm Ly}\alpha}/(4\pi c) = 2.02\times10^{-8}$ is a dimensionless quantity that includes the damping constant of the Lyα resonance (Λ_α) and the Lyα wavelength ($\lambda_{{\rm Ly}\alpha}$). This correction assumes that the IGM is uniformly distributed within the redshift range $z_{\rm IGM,l}$ to $z_{\rm IGM,u}$. We set the upper bound at the galaxy redshift, $z_{\rm IGM,u} = z_{\rm spec}$, and the lower bound to $z_{\rm IGM,l} = 5$. We fixed the BAGPIPES model's spectroscopic redshift to $z_{\rm spec}$ (i.e., the redshift of the galaxy) while keeping $z_{\rm abs}$ as a free parameter. We further assumed a double-power-law star formation history and Calzetti dust attenuation.

First, we attempted to model the DLA assuming an absorption redshift, $z_{\rm abs} = z_{\rm spec}$. The result is presented in Appendix B.1. Fixing $z_{\rm abs}$ to the spectroscopic redshift did not satisfactorily fit the data. Consequently, we retained the absorption redshift as a free parameter (see Table 2).

The best-fit SED model matched to the available spectroscopic and photometric data, with $z_{\rm abs}$ as a free parameter, is shown in Fig. 5. From the fit, we derived a stellar mass $\log(M_\star/M_\odot) = 7.80\pm0.01$, ionization parameter $\log U = -2.001^{+0.002}_{-0.001}$, and mass-weighted age of $\tau_{\rm mass} = (10.90^{+0.07}_{-0.12})$ Myr. The uncertainties represent the statistical errors from the posterior distribution of each quantity. Adopting different star-formation history or dust attenuation parametrizations induced an approximate systematic uncertainty of 0.3 dex on the stellar mass (see also Carnall et al. 2018).

The galaxy falls slightly above the star-forming main sequence (SFMS) of galaxies at $z \approx 6$ (Thorne et al. 2021; Heintz et al. 2023b). However, the stellar mass may be underestimated by 0.5 dex in our SED modeling due to "outshining" effects (Whitler et al. 2023; Giménez-Arteaga et al. 2023; Narayanan et al. 2024) concealing the more massive, older stellar population, which would place it consistently on the SFMS. As is clear from Fig. 5, we were not able to accurately constrain the damping as the large H I column density implied by the width of the damping wings is inconsistent with the rollover and absorption trough redshift. This was also noted by Cameron et al. (2023), motivating their modeling of the Lyα rollover as produced by two-photon emission. Here, we instead examined the parameter space, first assuming the simplest DLA scenario as outlined in Sect. 3.5.

Table 2. Physical properties of GS9422.

RA (J2000)	$03^{\rm h}32^{\rm m}29.2^{\rm s}$
Dec (J2000)	$-27°47'51.48''$
$z_{\rm spec}$	5.943 ± 0.001
$R_{\rm e}$ [kpc]	0.59
$A_{\rm e}$ [kpc^2]	1.85
$M_{\rm UV}$ [mag]	-19.56 ± 0.05
$L_{\rm UV}$ [erg s^{-1} Hz^{-1}]	$(3.15\pm0.16)\times10^{28}$
$\beta_{\rm UV}$	-2.36 ± 0.10
[O III] + Hβ EW [Å]	2266.4 ± 71.1
SFR$_{\rm H\alpha}$ [$M_\odot$ yr^{-1}]	8.2 ± 2.8
$\log\xi_{\rm ion}$ [Hz erg^{-1}]	25.62 ± 0.02
[a] $12+\log({\rm O/H})$	$7.58^{+0.05}_{-0.04}$
$\log(Z/Z_\odot)$	-1.13 ± 0.05
$T_{\rm e}$ [K]	$(1.6\pm0.15)\times10^4$
$f_{{\rm esc,Ly}\alpha}$	0.3 ± 0.2
[c] $\log(M_\star/M_\odot)$	7.80 ± 0.01
[c] $\tau_{\rm mass}$ [Myr]	$10.9^{+0.07}_{-0.12}$
[c] $\log U$	$-2.001^{+0.002}_{-0.001}$
[c] A_V [mag]	0.041 ± 0.013
[b] $z_{\rm abs}$	5.396 ± 0.098
[b] $\log(N_{\rm H\,I})$ [cm^{-2}]	23.68 ± 0.10
$\log\Sigma_{\rm SFR}$ [$M_\odot$ yr^{-1} kpc^{-2}]	1.14 ± 0.30
$\log\Sigma_{\rm gas}$ [$M_\odot$ pc^{-2}]	3.01 ± 0.01
[d] $\log(N_{\rm H\,I})$ [cm^{-2}]	22.94 ± 0.01
[d] $M_{\rm H\,I}$ [$M_\odot$]	$(1.27\pm0.03)\times10^9$
[d] $t_{\rm H\,I,depl.}$ [Gyr]	1.55 ± 0.53

Notes. Determined and measured physical properties of GS9422 (without values measured with BAGPIPES). [a]Derived following the procedure in Sanders et al. (2024). [b]From MCMC sampling. [c]Derived from the SED modeling with BAGPIPES. [d]Based on the Kennicutt-Schmidt law.

3.5. Lyα emission and DLA modeling

To model the continuum near the Lyα edge for an accurate measure of the DLA and Lyα emission feature, we described the rest-frame UV spectral shape with the model

$$F(\lambda) = F_0\lambda^{\beta_{\rm UV}}\times\tau_{\rm ISM}(\lambda) + \tau_{\rm IGM}(\lambda,z) \times\frac{f_{{\rm Ly}\alpha}}{\sqrt{2\pi}\sigma_{{\rm Ly}\alpha}}\exp\left(\frac{-(\lambda-\lambda_{{\rm Ly}\alpha,{\rm peak}})^2}{2\sigma^2}\right). \quad (7)$$

We found $\beta_{\rm UV} = -2.36\pm0.10$ and assumed this as the intrinsic continuum spectrum of the source. We superimposed the DLA feature and Lyα emission line described by a Gaussian on this model, assuming a prior on $z_{{\rm Ly}\alpha,{\rm em}} = z_{\rm spec}$, and left the DLA redshift, $z_{\rm abs}$, as a free parameter. In the fit, we masked out the two strongest identified UV emission lines from [C IV] and [C III]. We used Markov chain Monte Carlo (MCMC) through the `emcee` package to sample the posterior distribution of the modeled parameters. Corner plots of the full set of posterior distributions are shown in Figs. A.1 and A.2. We find that the redshift inferred for the Lyα emission is consistent with that derived from the longer-wavelength Balmer recombination lines, and fixed $z_{{\rm Ly}\alpha,{\rm em}} = z_{\rm spec}$ in the next iteration. The model parameter for the DLA redshift converges well on $z_{\rm abs} = 5.396\pm0.098$, with the full posterior distribution shown in Fig. 6. If this lower redshift solution for the DLA is robust, this would naturally

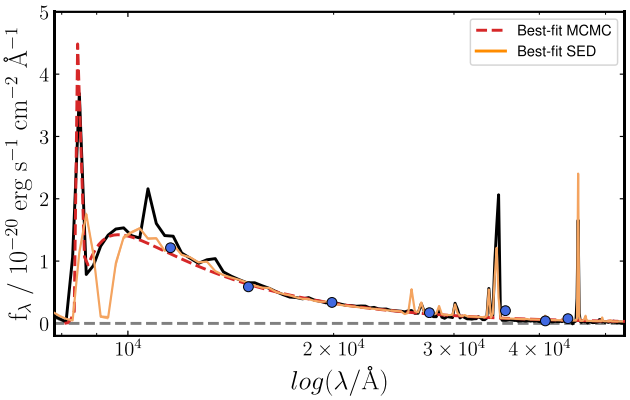

Fig. 5. Best-fit spectrophotometric SED and Lyα model of the JWST data. The black solid curve shows the JWST/NIRSpec Prism spectrum and the dark blue dots the corresponding JWST/NIRCam photometry. The best-fit SED model from BAGPIPES is shown as the orange curve, here modified to include the DLA, with z_{abs} as a free parameter. The best-fit MCMC stellar continuum and Lyα model is shown as the red dashed line, with a best-fit Lyα emission line redshift consistent with z_{spec} but $z_{abs} = 5.396 \pm 0.098$.

explain the simultaneous presence of a DLA feature and strong Lyα emission, which would be sufficiently outside the resonance frequency to not be entirely absorbed. We discuss the potential implications and provide a physical scenario in support of the lower-z solution in Sect. 4.

We measured the Lyα escape fraction as

$$f_{esc,Ly\alpha} = \frac{F_{obs,Ly\alpha}}{8.7 \times F_{obs,H\alpha}} \quad (8)$$

assuming an intrinsic Lyα/Hα ratio of 8.7 from the Case B recombination model and the inferred negligible dust component. This yields $f_{esc,Ly\alpha} = 0.3 \pm 0.2$, i.e., $\approx$30%, consistent with the general trend for faint ($M_{UV} < -19.5$ mag) galaxies at similar redshifts Saxena et al. (2024). This particular source thus likely represents the galaxy population that drives the large-scale reionization.

4. Interpreting the strong Lyman-α absorption and emission

To disentangle the potential contributions to the strong observed Lyα damping wings, we first considered multiple scenarios. First, the two-photon emission model presented by Cameron et al. (2023) appears to match the rest-frame UV data well and naturally explains the strong Lyα emission line as well. However, given that the derived electron temperatures and gas-phase metallicities are an order of magnitude lower or higher, respectively, than required by this model, we argue that this scenario is unlikely (as also argued by Chen et al. 2023). Second, an AGN can produce large UV-ionized proximity zones and thereby allow a substantial fraction of Lyα photons to escape, but since all our measurements are consistent with a typical star-forming galaxy at $z \sim 6$, we instead pursued the foreground DLA solution.

To disentangle the potential contributions to the observed Lyα damping wing, we first considered the SFR surface density, which we measured to be $\log(\Sigma_{SFR}/M_\odot\,yr^{-1}\,pc^{-2}) = 1.14 \pm 0.30$. This corresponds to a gas surface density of $\log(\Sigma_{gas}/M_\odot\,pc^{-2}) = 3.01 \pm 0.30$, assuming the locally derived Kennicutt–Schmidt (KS) relation (Kennicutt 1998; Heiderman et al. 2010; Kennicutt & Evans 2012). Converting this into a gas mass and assuming that $M_{HI} = 2/3\,M_{gas}$ (where the molecular gas mass constitutes $M_{H_2} = 1/3\,M_{gas}$) at $z \approx 6$ (Heintz et al. 2022), this yields $M_{HI} = 2/3\,\Sigma_{gas}A_e = (1.27 \pm 0.03) \times 10^9\,M_\odot$. This corresponds to an integrated H I column density of $N_{HI} = M_{HI}/(m_{HI}A_e) = (8.58 \pm 0.02) \times 10^{22}\,cm^{-2}$, where m_{HI} is the mass the hydrogen atom. This is an order of magnitude lower than the H I column density inferred from the strength of the Lyα damping wing and implies a H I gas mass fraction of $M_{HI}/M_\star = 0.20 \pm 0.01$ and a gas depletion time of $t_{depl,HI} = M_{HI}/SFR_{H\alpha} = 1.55 \pm 0.53$ Gyr. This supports the idea that there is an additional contribution to the integrated H I column density or potentially that the typical gas masses are underestimated by a factor of $\approx$10 in galaxies at $z \approx 6$ for a given SFR density compared to the locally calibrated KS relation. We argue that this is unlikely since this relation has been robustly validated up to $z \gtrsim 2$ (e.g., Danielson et al. 2011) and would imply a H I gas mass fraction of $M_{HI}/M_\star \approx 20$ for this particular source.

Instead, the most viable solution is that the DLA traces a dense H I gas reservoir in the foreground of the galaxy at $z = 5.40 \pm 0.10$. Naturally, this would also allow for substantial escaping Lyα emission as the resonance frequency of the transition is equally shifted to higher frequencies. Serendipitously, we note research reporting a massive galaxy overdensity at exactly $z = 5.4$ in nearby projection to the source presented here (Helton et al. 2023). The impact parameter to the center of the proposed galaxy protocluster corresponds to $\approx$0.9 pMpc at the cluster redshift, as illustrated in Fig. 6. This is well within typical galaxy clusters observed in the local Universe, such as Coma and Virgo, and indeed includes most of the cluster members at $z = 5.4$ (Helton et al. 2023). At lower redshifts, that is, $z \sim 2$–3, IGM H I overdensities have been revealed through Lyα absorption on background galaxy spectra and used to trace massive protoclusters (Frye et al. 2008; Cai et al. 2017), albeit at much lower column densities than inferred here. Intriguingly, this may imply that we are probing a dense, large-scale neutral gas reservoir connected to and feeding the formation of the galaxy protocluster members at $z = 5.4$, after the end of reionization. At higher redshifts, Chen et al. (2023) present circumstantial evidence for a similar scenario based on the presence of strong DLAs in a small set of galaxies near a galaxy overdensity at $z \approx 7.8$. However, the implied gas column and total H I gas mass for such a structure at $z = 5.4$ observed here is immense, since typically the intracluster medium is observed to be comprised of more diffuse gas and the large-scale IGM is expected to be fully ionized at this epoch. An alternative scenario could be that the measured H I column density is the cumulative representation of multiple DLAs along the line of sight from the galaxy redshift to the foreground absorber (see e.g., Witstok et al. 2024). To fully corroborate this scenario and potentially measure the covering fraction and total CCM H I mass, we need larger statistical samples and sight lines at different impact parameters through these clusters.

5. Conclusion

We have presented a comprehensive characterization of the stellar and gas-phase content of a galaxy near the end of the reionization era showing an anomalous superposition of both a strong Lyα emission line and a broadened DLA wing. This particular source was observed as part of the JADES GTO survey, for which medium-resolution ($\mathcal{R} \approx 1000$) JWST/NIRSpec grating and Prism-mode spectra and multi-band NIRCam imaging have been obtained. From the multitude of detected nebular emission

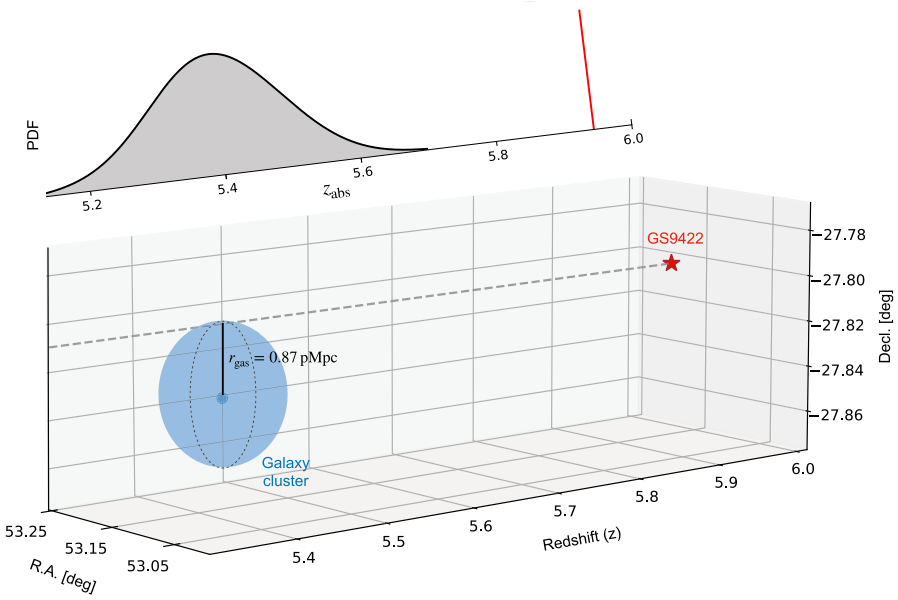

Fig. 6. 3D illustration of the proposed scenario with GS9244 at $z = 5.943$ being in the background of a galaxy-cluster overdensity at $z = 5.4$. The estimated center and mean redshift of the cluster is marked by the small blue dot (Helton et al. 2023), and the blue sphere with radius $r = 0.87$ pMpc shows the impact parameter to the galaxy sight line. The smoothed probability density function from the MCMC analysis (Fig. A.2) is shown at the top, distributed around the cluster redshift with median $z = 5.4$.

lines, we measured the redshift to be $z_{spec} = 5.943 \pm 0.001$ and find the source to be actively forming stars at SFR $= (8.20 \pm 2.8)\,M_\odot\,\mathrm{yr}^{-1}$ with a Lyα escape fraction of $f_{esc,Ly\alpha} = 30\%$. Based on the detection of the auroral [O III] λ4363 emission line, we further determined the electron temperature of the H II region to be $T_e = (1.60 \pm 0.15) \times 10^4$ K, which allowed us to accurately measure the oxygen gas-phase abundance to be $12 + \log(\mathrm{O/H}) = 7.78 \pm 0.10$ via the direct T_e method. This source thus appears as a typical, albeit highly intense, star-forming galaxy at $z \approx 6$.

To model the observed SED and Lyα emission and broad DLA trough, we modified the default capabilities of the SED fitting tool BAGPIPES (Carnall et al. 2018) in order to include a prescription for the Lyα transmission for a given H I column density, N_{HI}. This yields a dust-poor ($A_V = (0.041 \pm 0.013)$ mag), young (age ≈ 11 Myr) star-forming galaxy with a stellar mass of $\log(M_\star/M_\odot) = 7.80 \pm 0.01$. The posterior distributions suggest an abundant H I column density with $N_{HI} > 10^{23}\,\mathrm{cm}^{-2}$, although this did not correlate well with the data. Instead, we modeled the Lyα region independently using an MCMC to sample the posterior distribution of the absorber. We found a lower-redshift solution $z_{abs} = 5.40 \pm 0.10$, inconsistent with the galaxy redshift at $>3\sigma$ confidence, that qualitatively provided a much better fit to the data.

We demonstrated via the KS relation and based on the measured SFR surface density, $\log(\Sigma_{SFR}/M_\odot\,\mathrm{yr}^{-1}\,\mathrm{kpc}^{-2}) = 1.14 \pm 0.30$, that the galaxy itself is likely only contributing to $\lesssim$10% of the integrated H I gas column along the line of sight. This was further evidence that the majority of the H I gas is located in the foreground and not physically associated with the galaxy. Intriguingly, a recent study by Helton et al. (2023) reports a massive galaxy overdensity located at $z = 5.387$ within a nearby ($\approx$1 Mpc) projected distance to the galaxy studied here. This scenario would also naturally resolve the simultaneous detection of strong Lyα emission and abundant, self-shielding H I columns probed via the DLA feature. While larger statistical samples and sight lines are needed to validate this scenario, this interpretation is intriguing and introduces some ambiguity into the interpretations that two-photon nebular emission (Cameron et al. 2023) or the AGN+young stellar disk interpretations are the dominant contributions to the rest-frame UV spectral continuum.

Acknowledgements. We would like to thank the referee for providing a constructive and timely report, greatly improving the presentation of the results in this work. We would like to thank Harley Katz for enlightening discussions on the physical interpretation of the two-photon emission model. This work has received funding from the Swiss State Secretariat for Education, Research and Innovation (SERI) under contract number MB22.00072. The Cosmic Dawn Center (DAWN) is funded by the Danish National Research Foundation under grant DNRF140. The data products presented herein were retrieved from the DAWN JWST Archive (DJA). DJA is an initiative of the Cosmic Dawn Center, which is funded by the Danish National Research Foundation under grant DNRF140. This work is based in part on observations made with the NASA/ESA/CSA James Webb Space Telescope. The data were obtained from the Mikulski Archive for Space Telescopes (MAST) at the Space Telescope Science Institute, which is operated by the Association of Universities for Research in Astronomy, Inc., under NASA contract NAS 5-03127 for JWST.

References

Arellano-Córdova, K. Z., Berg, D. A., Chisholm, J., et al. 2022, ApJ, 940, L23
Asplund, M., Grevesse, N., Sauval, A. J., & Scott, P. 2009, ARA&A, 47, 481
Atek, H., Labbé, I., Furtak, L. J., et al. 2023, ArXiv e-prints [arXiv:2308.08540]
Bouwens, R. J., Smit, R., Labbé, I., et al. 2016, ApJ, 831, 176
Brammer, G. 2023, https://doi.org/10.5281/zenodo.7299500
Brammer, G., Strait, V., Matharu, J., & Momcheva, I. 2022, https://doi.org/10.5281/zenodo.6672538
Brinchmann, J. 2023, MNRAS, 525, 2087
Bunker, A. J., Saxena, A., Cameron, A. J., et al. 2023, A&A, 677, A88
Bunker, A. J., Cameron, A. J., Curtis-Lake, E., et al. 2024, A&A, in press, https://doi.org/10.1051/0004-6361/202347094
Cai, Z., Fan, X., Bian, F., et al. 2017, ApJ, 839, 131
Calabro, A., Castellano, M., Zavala, J. A., et al. 2024, ArXiv e-prints [arXiv:2403.12683]
Cameron, A. J., Katz, H., Witten, C., et al. 2023, ArXiv e-prints [arXiv:2311.02051]
Carnall, A. C., McLure, R. J., Dunlop, J. S., & Davé, R. 2018, MNRAS, 480, 4379
Chen, Z., Stark, D. P., Mason, C., et al. 2023, ArXiv e-prints [arXiv:2311.13683]
Curti, M., D'Eugenio, F., Carniani, S., et al. 2023, MNRAS, 518, 425
Curti, M., Maiolino, R., Curtis-Lake, E., et al. 2024, A&A, 684, A75
Curtis-Lake, E., Carniani, S., Cameron, A., et al. 2023, Nat. Astron., 7, 622
Danielson, A. L. R., Swinbank, A. M., Smail, I., et al. 2011, MNRAS, 410, 1687
D'Eugenio, F., Maiolino, R., Carniani, S., et al. 2024, A&A, 689, A152
Eisenstein, D. J., Willott, C., Alberts, S., et al. 2023, ArXiv e-prints [arXiv:2306.02465]
Erb, D. K., Berg, D. A., Auger, M. W., et al. 2019, ApJ, 884, 7
Frye, B. L., Bowen, D. V., Hurley, M., et al. 2008, ApJ, 685, L5

Fujimoto, S., Wang, B., Weaver, J., et al. 2023, ArXiv e-prints [arXiv:2308.11609]
Giménez-Arteaga, C., Oesch, P. A., Brammer, G. B., et al. 2023, ApJ, 948, 126
Heiderman, A., Evans, N. J., Allen, L. E., Huard, T., & Heyer, M. 2010, ApJ, 723, 1019
Heintz, K. E., Oesch, P. A., Aravena, M., et al. 2022, ApJ, 934, L27
Heintz, K. E., Giménez-Arteaga, C., Fujimoto, S., et al. 2023a, ApJ, 944, L30
Heintz, K. E., Brammer, G. B., Giménez-Arteaga, C., et al. 2023b, Nat. Astron., 7, 1517
Heintz, K. E., Watson, D., Brammer, G., et al. 2024a, Science, 384, 890
Heintz, K. E., Brammer, G. B., Watson, D., et al. 2024b, A&A, submitted [arXiv:2404.02211]
Helton, J. M., Sun, F., Woodrum, C., et al. 2023, ArXiv e-prints [arXiv:2302.10217]
Izotov, Y. I., Stasińska, G., Meynet, G., Guseva, N. G., & Thuan, T. X. 2006, A&A, 448, 955
Jakobsen, P., Ferruit, P., Alves de Oliveira, C., et al. 2022, A&A, 661, A80
James, B. L., Aloisi, A., Heckman, T., Sohn, S. T., & Wolfe, M. A. 2014, ApJ, 795, 109
Katz, H., Saxena, A., Cameron, A. J., et al. 2023, MNRAS, 518, 592
Keating, L. C., Bolton, J. S., Cullen, F., et al. 2023, ArXiv e-prints [arXiv:2308.05800]
Kennicutt, R. C. 1998, ARA&A, 36, 189
Kennicutt, R. C., & Evans, N. J. 2012, ARA&A, 50, 531
Kewley, L. J., Dopita, M. A., Sutherland, R. S., Heisler, C. A., & Trevena, J. 2001, ApJ, 556, 121
Kroupa, P. 2001, MNRAS, 322, 231
Langeroodi, D., Hjorth, J., Chen, W., et al. 2023, ApJ, 957, 39
Li, Y., Leja, J., Johnson, B. D., Tacchella, S., & Naidu, R. P. 2024, ArXiv e-prints [arXiv:2404.02333]
Lin, X., Cai, Z., Zou, S., et al. 2023, ApJ, 944, L59
Matthee, J., Mackenzie, R., Simcoe, R. A., et al. 2023, ApJ, 950, 67
McQuinn, M., Lidz, A., Zaldarriaga, M., Hernquist, L., & Dutta, S. 2008, MNRAS, 388, 1101
Miralda-Escudé, J. 1998, ApJ, 501, 15
Miralda-Escude, J., Haehnelt, M., & Rees, M. J. 2000, ApJ, 530, 1
Nakajima, K., Ouchi, M., Isobe, Y., et al. 2023, ApJS, 269, 33
Narayanan, D., Lower, S., Torrey, P., et al. 2024, ApJ, 961, 73
Osterbrock, D. E., & Ferland, G. J. 2006, Astrophysics of Gaseous Nebulae and Active Galactic Nuclei (Sausalito: University Science Books)
Planck Collaboration VI. 2020, A&A, 641, A6
Rhoads, J. E., Wold, I. G. B., Harish, S., et al. 2023, ApJ, 942, L14
Rieke, M. J., Kelly, D. M., Misselt, K., et al. 2023, PASP, 135, 028001
Robertson, B. E. 2022, ARA&A, 60, 121
Robertson, B. E., Furlanetto, S. R., Schneider, E., et al. 2013, ApJ, 768, 71
Sanders, R. L., Shapley, A. E., Topping, M. W., Reddy, N. A., & Brammer, G. B. 2024, ApJ, 962, 24
Saxena, A., Bunker, A. J., Jones, G. C., et al. 2024, A&A, 684, A84
Schaerer, D. 2003, A&A, 397, 527
Schaerer, D., Marques-Chaves, R., Barrufet, L., et al. 2022, A&A, 665, L4
Scholtz, J., Maiolino, R., D'Eugenio, F., et al. 2023, A&A, submitted [arXiv:2311.18731]
Shapley, A. E., Steidel, C. C., Pettini, M., & Adelberger, K. L. 2003, ApJ, 588, 65
Steinhardt, C. L., Kokorev, V., Rusakov, V., Garcia, E., & Sneppen, A. 2023, ApJ, 951, L40
Tacchella, S., McClymont, W., Scholtz, J., et al. 2024, ArXiv e-prints [arXiv:2404.02194]
Taylor, A. J., Barger, A. J., & Cowie, L. L. 2022, ApJ, 939, L3
Tepper-García, T. 2006, MNRAS, 369, 2025
Thorne, J. E., Robotham, A. S. G., Davies, L. J. M., et al. 2021, MNRAS, 505, 540
Totani, T., Kawai, N., Kosugi, G., et al. 2006, PASJ, 58, 485
Trump, J. R., Arrabal Haro, P., Simons, R. C., et al. 2023, ApJ, 945, 35
Übler, H., Maiolino, R., Curtis-Lake, E., et al. 2023, A&A, 677, A145
Umeda, H., Ouchi, M., Nakajima, K., et al. 2023, ArXiv e-prints [arXiv:2306.00487]
Valentino, F., Brammer, G., Gould, K. M. L., et al. 2023, ApJ, 947, 20
Wang, B., Fujimoto, S., Labbe, I., et al. 2023, ArXiv e-prints [arXiv:2308.03745]
Whitler, L., Stark, D. P., Endsley, R., et al. 2023, MNRAS, 519, 5859
Witstok, J., Smit, R., Saxena, A., et al. 2024, A&A, 682, A40

Appendix A: Posterior distributions

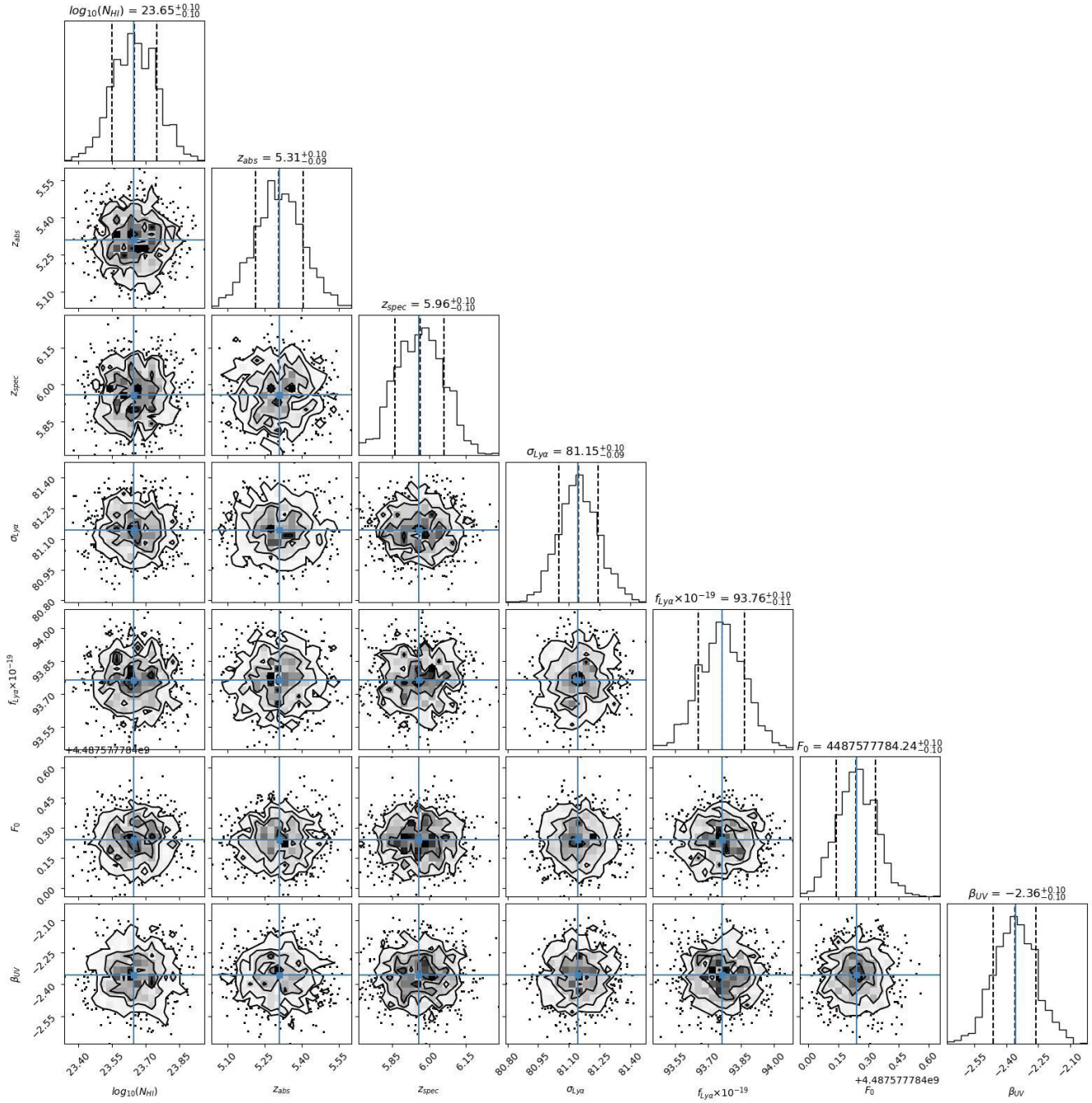

Fig. A.1. Cornerplot for MCMC fit with *no* fixed parameters.

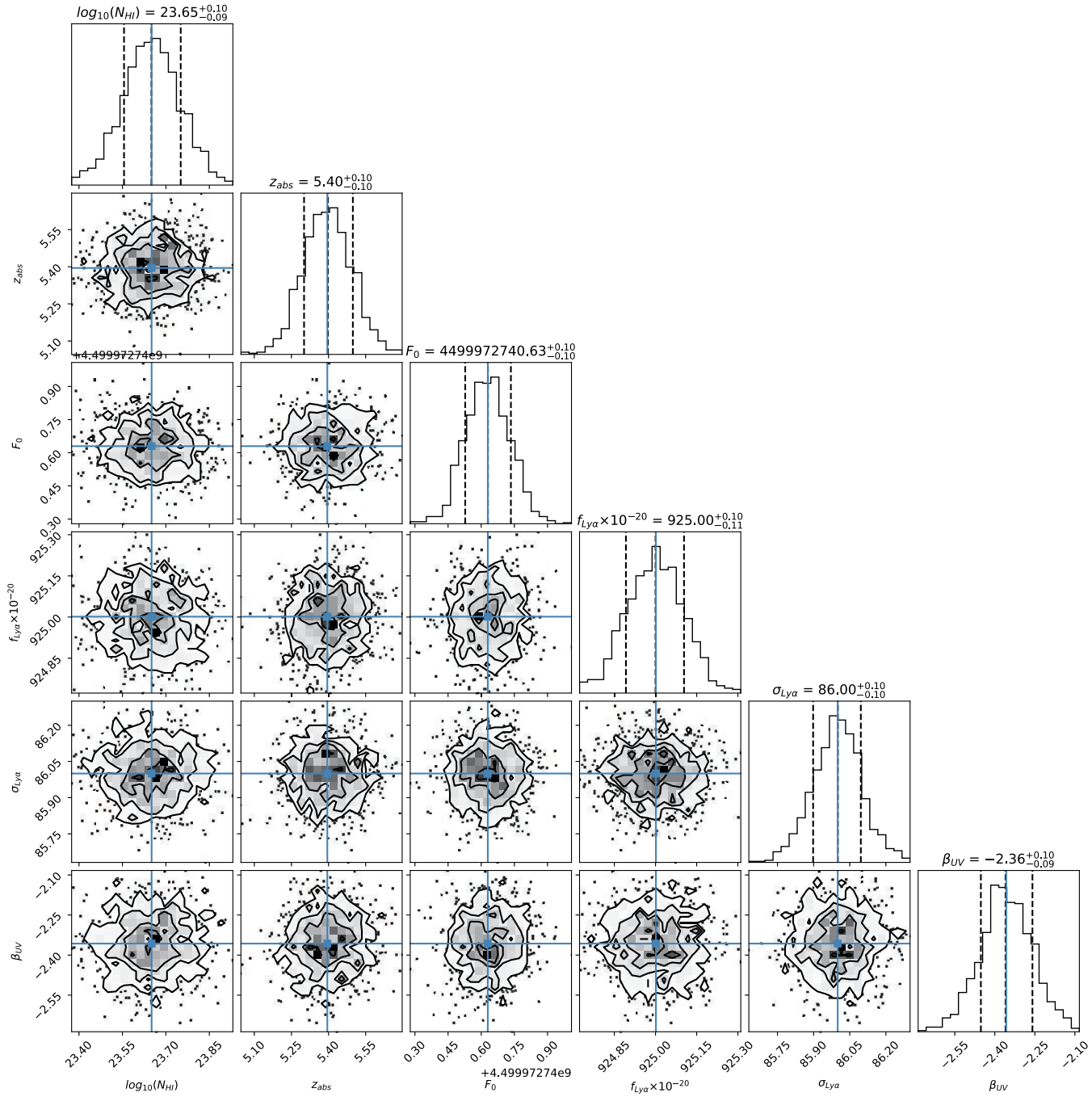

Fig. A.2. Cornerplot for MCMC fit with $z_{\mathrm{Ly}\alpha,\mathrm{em}} = z_{\mathrm{spec}}$ (fixed) and z_{abs} as a free parameter.

Appendix B: SED fitting with $z_{\rm abs} = z_{\rm spec}$

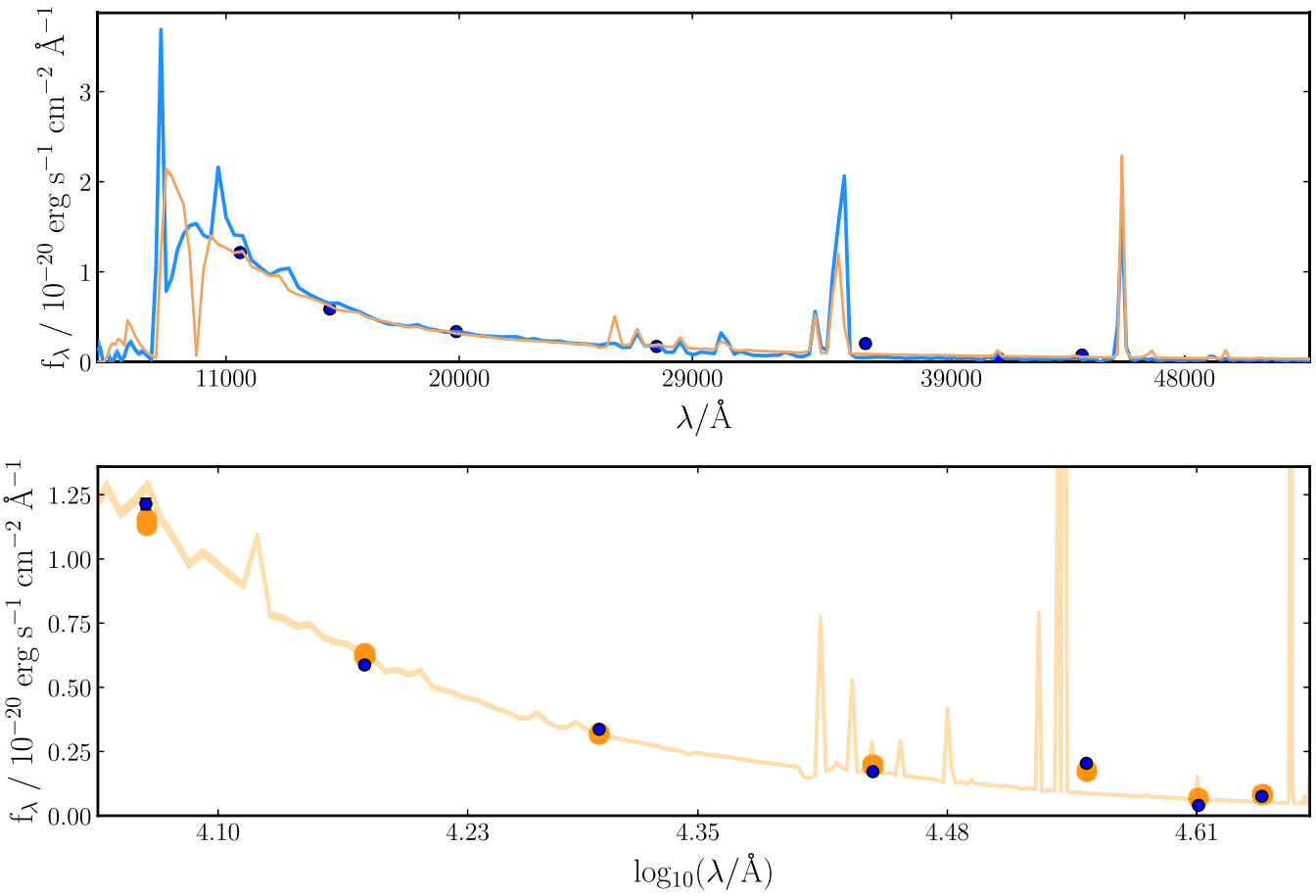

Fig. B.1. Best-fit SED model matched to both spectroscopic and photometric data with $z_{\rm abs} = z_{\rm spec}$.